Article

Nano-Cellulose/MOF Derived Carbon Doped CuO/Fe$_3$O$_4$ Nanocomposite as High Efficient Catalyst for Organic Pollutant Remedy

Hailong Lu [1,2], Lili Zhang [1,2], Jinxia Ma [1], Nur Alam [2], Xiaofan Zhou [1,]* and Yonghao Ni [2,]*

[1] National-Provincial Joint Engineering Research Center of Electromechanical Product Packaging, Jiangsu Co-Innovation Center of Efficient Processing and Utilization of Forest Resources, Nanjing Forestry University, Nanjing 210037, China; 15298393737@163.com (H.L.); luo913302@163.com (L.Z.); jxma@njfu.edu.cn (J.M.)

[2] Department of Chemical Engineering, University of New Brunswick, Fredericton, NB E3B 5A3, Canada; malam6@unb.ca

[*] Correspondence: zxiaofan@njfu.com.cn (X.Z.); yonghao@unb.ca (Y.N.); Tel.: +86-25-85428932 (X.Z.); +1-506-451-6857 (Y.N.); Fax: +86-25-85428932 (X.Z.); +1-506-453-4767 (Y.N.)

check for updates

Abstract: Metal–organic framework (MOF)-based derivatives are attracting increased interest in various research fields. In this study, nano-cellulose MOF-derived carbon-doped CuO/Fe$_3$O$_4$ nanocomposites were successfully synthesized via direct calcination of magnetic Cu-BTC MOF (HKUST-1)/Fe$_3$O$_4$/cellulose microfibril (CMF) composites in air. The morphology, structure, and porous properties of carbon-doped CuO/Fe$_3$O$_4$ nanocomposites were characterized using SEM, TEM, powder X-ray diffraction (PXRD), X-ray photoelectron spectroscopy (XPS), and vibrating sample magnetometry (VSM). The results show that the as-prepared nanocomposite catalyst is composed of Fe$_3$O$_4$, CuO, and carbon. Compared to the CuO/Fe$_3$O$_4$ catalyst from HKUST-1/Fe$_3$O$_4$ composite and CuO from HKUST-1, this carbon-doped CuO/Fe$_3$O$_4$ nanocomposite catalyst shows better catalytic efficiency in reduction reactions of 4-nitrophenol (4-NP), methylene blue (MB), and methyl orange (MO) in the presence of NaBH$_4$. The enhanced catalytic performance of carbon-doped CuO/Fe$_3$O$_4$ is attributed to effects of carbon preventing the aggregation of CuO/Fe$_3$O$_4$ and providing high surface-to-volume ratio and chemical stability. Moreover, this nanocomposite catalyst is readily recoverable using an external magnet due to its superparamagnetic behavior. The recyclability/reuse of carbon-doped CuO/Fe$_3$O$_4$ was also investigated.

Keywords: nano-cellulose; MOF; carbon-doped CuO/Fe$_3$O$_4$ nanocatalyst; catalytic reduction; pollutant remedy

1. Introduction

Recently, metal nanoparticles (NPs) were widely used in the fields of biomedicine and chemical reactions due to their high selectivity and catalytic efficiency [1–3]. Noble-metal nanoparticles (gold, silver, etc.) [4–6] and non-noble-metal nanoparticles (copper, zinc, and their oxides, sulfides, etc.) [7–10] are particularly noticeable. For example, Jiang et al. [11] reported that CuO and Au domains could greatly improve the photocatalytic activity and stability of Cu$_2$O cubes in the photocatalytic degradation of methyl orange (MO). Rodríguez et al. [12] reported that potassium poly(heptazine imide) (PHIK)/Ti-based metal–organic framework (MIL-125-NH$_2$) composites had superior photocatalytic activity in rhodamine B (RhB) degradation under blue-light irradiation. Among the applications, metal nanoparticles can also be used for treating wastewater and drinking water due to their large surface areas and high activity [13,14]. With growing focus on the development

of cost-effective, efficient catalysts, more attention is being paid to non-noble-metal catalysts, such as metal-oxide catalysts.

Metal NPs with nanometer-scale dimensions are unstable and tend to aggregate due to their high surface energy and surface area, which can lead to the loss of catalytic efficiency [15–17]. The concept of immobilization/stabilization of metal NPs onto support/substrates is one of the effective methods to overcome aggregation of NPs [18,19]. There are many types of substrates/matrices that can be used to support metal NPs, such as carbon [20,21], silica [22], metal oxide [23], polymers, etc. [24–26]. Carbon, as a support for metal nanoparticles, provides multiple accessible channels for diffusion/transport to take advantage of the excellent catalytic functionalities of metal nanoparticles [27].

In past decades, metal–organic frameworks (MOFs) attracted much attention due to their porous structures and potential applications in gas storage, molecule separation, chemical sensing, drug delivery, and catalysis [28–30]. Recently, MOF-based derivative catalysts received more attention because MOF-derived materials have advantages in terms of tailorable morphologies, hierarchical porosity, and easy functionalization with other heteroatoms and metal oxides [31,32]. For instance, Ji et al. used ZIF-67 as a precursor to synthesize a Pt@Co_3O_4 composite to improve the catalytic activity of CO oxidation [33]. Yang et al. reported that ZnO nanoparticles prepared via calcination of MOF-5 in air at 600 °C showed excellent photocatalytic degradation of rhodamine B [34]. Niu et al. synthesized a hybrid catalyst consisting of Cu/Cu_2O NPs supported on porous carbon for the catalytic reduction of 4-nitrophenol (4-NP) using HKUST-1 as a precursor [27].

The direct pyrolysis/thermolysis treatment of MOFs is a simple and controllable method to prepare various metal oxides in a one-step process. By following it, we can successfully synthesize carbon-doped CuO/Fe_3O_4 composite catalysts for organic pollutant reduction. Herein, we prepared carbon-doped CuO/Fe_3O_4 composite catalysts via direct calcination of HKUST-1/Fe_3O_4/CMF composites under air. We then applied the as-prepared carbon-doped CuO/Fe_3O_4 composite catalysts for the catalytic reduction of 4-NP. Its catalytic performance, in comparison with a CuO/Fe_3O_4 composite from HKUST-1/Fe_3O_4 composite and CuO, is remarkably better, which is attributed to the fact that carbon doping can (1) minimize the aggregation of CuO/Fe_3O_4, (2) provide high surface-to-volume ratio and chemical stability for the catalyst in contact with the target pollutants, and (3) enhance the catalytic activity of the CuO/Fe_3O_4 catalyst. Furthermore, the carbon-doped CuO/Fe_3O_4 composite catalyst has excellent efficiency in the reduction of methylene blue (MB) and methyl orange (MO). The features of the carbon-doped CuO/Fe_3O_4 composite catalyst are as follows: CuO acts as the effective catalyst, with the doped carbon having the three functions discussed, and the magnetic Fe_3O_4 supports easy reuse/recycling of the catalyst using a magnet.

2. Experimental

2.1. Materials

Cellulose microfibrils (CMF) (~4.0 wt.%) from Cellulose Lab; trimesic acid (H_3BTC), copper (II) acetate monohydrate, ethanol, and hydrochloric acid (HCl, 37%, *w/w*) from Sigma-Aldrich; methylene blue, ferric nitrate nonahydrate (Fe($NO_3)_3 \cdot 9H_2O$), ferrous sulfate (FeSO$_4 \cdot 7H_2O$), citric acid anhydrous, and sodium hydroxide (NaOH, 50%, *w/w*) from Fisher Scientific were used in this study. All other chemicals were of analytical grade and used without further purification.

2.2. Synthesis of Magnetic Carbon-Doped CuO/Fe₃O₄ Nanocomposite Catalyst

Fe_3O_4/cellulose microfibril (CMF) composites were prepared using chemical co-precipitation of aqueous ferrous and ferric ions, and the procedures were similar to those described in the literature [35]. CMF (7.5 g, ~4%, *w/w*) was diluted to 0.3 wt.% with distilled water and stirred for 5 min at 1000 rpm. The diluted CMF suspension was further treated in a sonicator (QSON-ICA) for 5 min to disperse the individual nanocellulose, followed by heating at 65 °C and bubbling with nitrogen for

10 min under magnetic stirring (500 rpm) to remove the dissolved oxygen from the CMF suspension. Then, citric acid (1 mg) and diluted HCl solution (1 mL, 2 mol/L) were added to the above solution, followed by the successive additions of 1.3 mmol $Fe(NO_3)_3 \cdot 9H_2O$ and 0.65 mmol $FeSO_4 \cdot 7H_2O$ solid samples with nitrogen bubbling and magnetic stirring. The function of citric acid was to protect the as-prepared Fe_3O_4 NPs from being oxidized by the dissolving oxygen in water. A dilute NaOH solution (10 mL, 2 mol/L) was added drop-wise into the above system, followed by bubbling with nitrogen and magnetic stirring (500 rpm) for 120 min at room temperature. The obtained Fe_3O_4/CMF composites (using a magnet) were washed three times with distilled water in a centrifugation step (4000 rpm, 10 min).

Copper (II) acetate monohydrate was dissolved in distilled water. Fe_3O_4/CMF nanocomposites and H_3BTC were dispersed in ethanol and then treated in a sonicator (QSON-ICA) for 5 min. The ethanol solution containing Fe_3O_4/CMF composite and H_3BTC was added to the aqueous system. The color of the solution changed from light blue to blue-black immediately, and the system was stirred continuously for 4 h. The final HKUST-1/Fe_3O_4/CMF composite was washed in a centrifugation step (4000 rpm, 10 min) with distilled water and absolute ethanol three times. Then, the drying was done at 50 °C under vacuum.

The synthesized HKUST-1/Fe_3O_4/CMF composites were placed in a ceramic boat, then transferred to a muffle roaster, which was operated under the conditions of 500 °C, air atmosphere, and a heating rate of 20 °C/min, before being held at 500 °C for 5 h; the procedures were similar to those described in the literature [36]. After cooling to room temperature, the sample was washed several times with distilled water and absolute ethanol in a centrifugation step (4000 rpm, 10 min), and finally dried in a vacuum at 60 °C for 5 h.

2.3. Characterization

Transmission electron microscope (TEM) analyses were conducted with a JEOL JEM 2011 transmission electron microscope at 200 kV. Scanning electron microscope (SEM) analyses were conducted with a JEOL JSM 6400 scanning electron microscope. The powder X-ray diffraction (PXRD) patterns of the prepared samples were collected using an X-ray diffractometer with Cu-Kα radiation (40 kV, 30 mA). The patterns were recorded in the region of 2θ from 10° to 80° with a scan step of 0.02°. The chemical binding energies of the respective ions in the samples were measured using X-ray photoelectron spectroscopy (XPS, ESCALa-b220i-XL electron spectrometer, Thermo Fisher Scientific K-Alpha, UK) under 300-W Al-Kα radiation. The magnetic properties were measured with a vibrating sample magnetometer (VSM), a physical property measurement system, at 300 K, as a function of the applied magnetic field between −80 and 80 kOe. The ultraviolet–visible (UV–Vis) diffuse reflectance data were collected with a UV–Vis spectrophotometer (Evolution 201, Thermo Scientific) equipped with an integrated sphere.

2.4. Evaluation of Catalytic Performance

The catalytic reduction of 4-nitrophenol (4-NP) using $NaBH_4$ was chosen as the model reaction for investigating the catalytic performance of magnetic carbon-doped CuO/Fe_3O_4 nanocomposite catalysts. Typically, catalytic reduction of a 30-mL 4-NP solution (1 mmol/L) was carried out in a beaker (100 mL) by continuously stirring at room temperature. Upon the addition of $NaBH_4$ (10 mM) into the 4-NP solution, its color changed immediately from light yellow to dark yellow due to the formation of 4-nitrophenolate ions (formed from the high alkalinity of $NaBH_4$) [37]. Then, the dark-yellow color faded with time (due to the conversion of 4-NP to 4-aminophenol (4-AP)) after the addition of carbon-doped CuO/Fe_3O_4 nanocomposite catalyst (5 mg) (Scheme 1). UV–Vis adsorption spectra were recorded using a UV–Vis spectrophotometer in the range of 250–550 nm. When the reaction completed, the catalyst was easily separated from the solution using an external magnet due to its good magnetic performance.
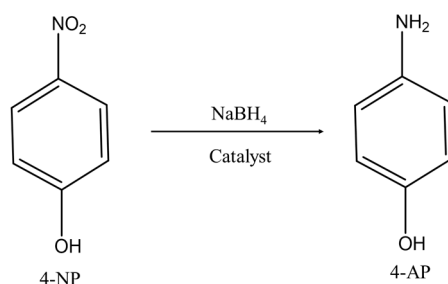
Scheme 1. Catalytic reduction of 4-nitrophenol to 4-aminophenol.

During the degradation process of organic dyes, 30 mL of dye solution (10 mg/L) and $NaBH_4$ (10 mM) were mixed in a beaker (100 mL) by continuously stirring at room temperature. Then, 5 mg of carbon-doped CuO/Fe_3O_4 nanocomposite catalyst was added to the reaction system, and the catalytic process was monitored using the UV–Vis spectrophotometer. When the reaction ended, the catalyst was readily separated from the solution using an external magnet.

3. Results and Discussion

3.1. Structure and Morphological Characterization

MOFs can be readily converted to metal-oxide composites, which take advantage of their original morphology and porosity. The as-prepared HKUST-1, HKUST-1/Fe_3O_4, and HKUST-1/Fe_3O_4/CMF composite samples were then calcinated to obtain the nanoporous metal-oxide particles, generating nanoporous CuO, CuO/Fe_3O_4, and carbon-doped CuO/Fe_3O_4 composite catalysts, respectively. Pyrolysis/thermolysis of HKUST-1/Fe_3O_4/CMF composites led to the formation of porous carbon-doped CuO/Fe_3O_4 composites.

The size and the morphology of the synthesized materials were investigated using a transmission electron microscope (TEM) and scanning electron microscope (SEM). Figure 1 shows the SEM and TEM images of HKUST-1/Fe_3O_4/CMF composites and carbon-doped CuO/Fe_3O_4 composites after calcination in air. HKUST-1 crystals and Fe_3O_4 nanoparticles were uniformly loaded onto the surface of CMF (Figure 1). The nanocellulose MOF-derived porous carbon-doped CuO/Fe_3O_4 composite was then obtained through a calcination process under air at 500 °C for 5 h. The Brunauer–Emmett–Teller surface area (S_{BET}) of the carbon-doped CuO/Fe_3O_4 sample was 38.7 m^2/g, which was much higher than that of the CuO/Fe_3O_4 sample (0.042 m^2/g) obtained from the calcination of HKUST-1/Fe_3O_4. The resultant carbon-doped CuO/Fe_3O_4 composite inherited largely the original porous morphology of HKUST-1. Based on the mapping images, the conclusion was that both Cu and Fe elements dispersed well in the carbon-doped CuO/Fe_3O_4 composite catalyst.

XPS analysis was employed to investigate the elemental composition on the surface of different composites. For the XPS spectrum of carbon-doped CuO/Fe_3O_4 composite catalyst (Figure 2a), the main peaks were C*1s*, O*1s*, Fe*2p*, and Cu*2p*, centered at around 285 eV, 530 eV, 720 eV, and 930 eV, respectively. The C*1s* XPS pattern of the sample is shown in Figure 2b. The spectrum contains two peaks at 285 eV and 288.5 eV, which may be attributed to carbon (sp^2 hybridization) in the sample, and the Cu–O–C bonds or Fe–O–C bonds, respectively. Figure 2c shows the Cu*2p* core-level XPS spectrum of the composite catalyst. The Cu*2p1* and Cu*2p3* binding energies for the composite catalyst were 952.8 and 932.7 eV, respectively, indicating the presence of CuO in the composite catalyst. Similar results were reported in the literature [38,39]. The Fe*2p3* and Fe*2p1* binding energies (Figure 2d) for the composite catalyst were 710.7 and 725.4 eV, respectively, which agrees with published results [35,40], confirming the presence of Fe_3O_4 in the composite catalyst.
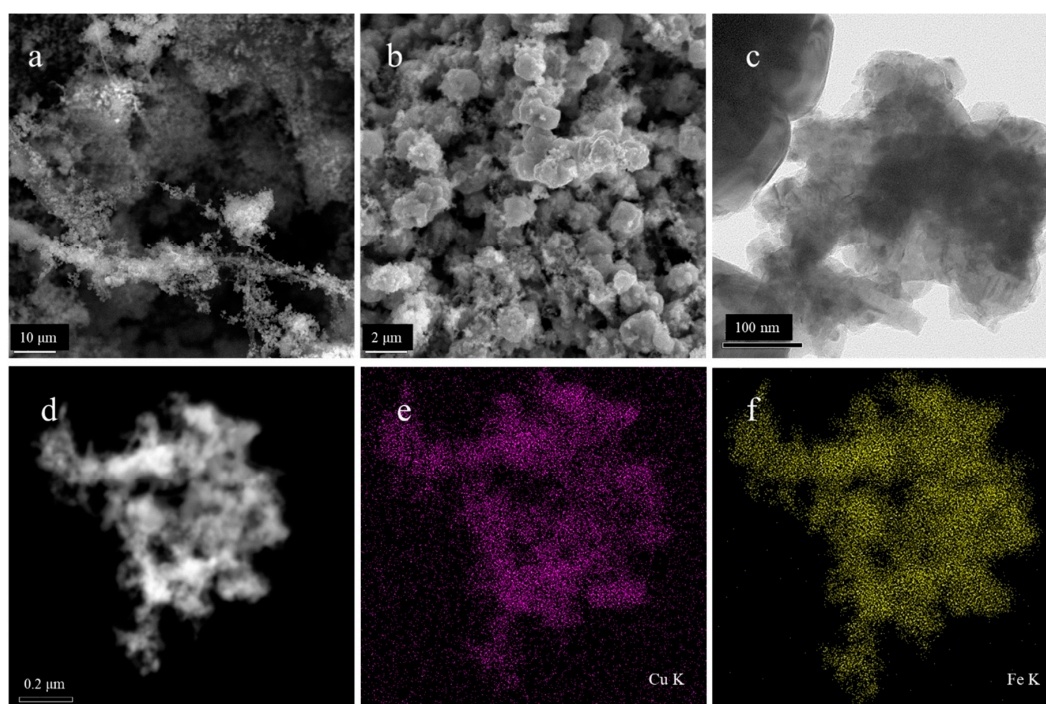
Figure 1. SEM images of (**a**) HKUST-1/Fe$_3$O$_4$/cellulose microfibril (CMF) composites and (**b**) carbon-doped CuO/Fe$_3$O$_4$ composite catalysts after calcination; TEM images of (**c**) carbon-doped CuO/Fe$_3$O$_4$ composite catalysts; (**d**–**f**) energy-dispersive X-ray spectroscopy (EDX) mapping of carbon-doped CuO/Fe$_3$O$_4$ composite catalysts.
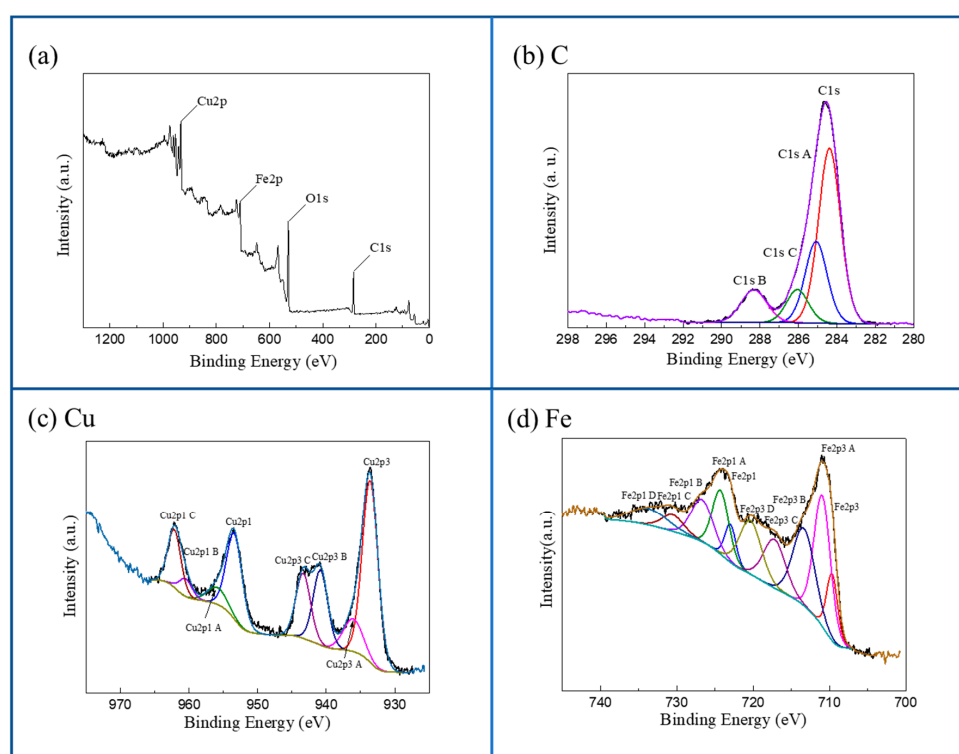

Figure 2. (**a**) High-resolution X-ray photoelectron spectroscopy (XPS) survey spectra of the carbon-doped CuO/Fe$_3$O$_4$ composite catalysts. (**b**) High-resolution XPS scans over C*1s* peaks of the carbon-doped CuO/Fe$_3$O$_4$ composite catalysts. (**c**) High-resolution XPS scans over Cu*2p* peaks of carbon-doped CuO/Fe$_3$O$_4$ composite catalysts. (**d**) High-resolution XPS scans over Fe*2p* peaks of carbon-doped CuO/Fe$_3$O$_4$ composite catalysts.

The crystalline nature and the composition of the as-synthesized products were characterized using PXRD. The crystalline phases of CuO, such as (110), (11-1), (111), (20-2), (020), (202), (11-3), (31-1), and (220) are shown in Figure 3a, which are consistent with those reported in the literature [41,42]. These results support the conclusion that HKUST-1 was transformed into CuO via calcination under the present conditions. In the XRD pattern of carbon-doped CuO/Fe_3O_4 composite, the diffraction peaks and relative intensities were indexed to Fe_3O_4 (JCPD NO. 19-0629) and CuO (JCPD NO. 05-0661). This indicates that CuO and Fe_3O_4 were both obtained via calcining HKUST-1/Fe_3O_4/CMF composites under air. No other C-related impurity peaks were detected; a similar result was reported in the previous research [43].
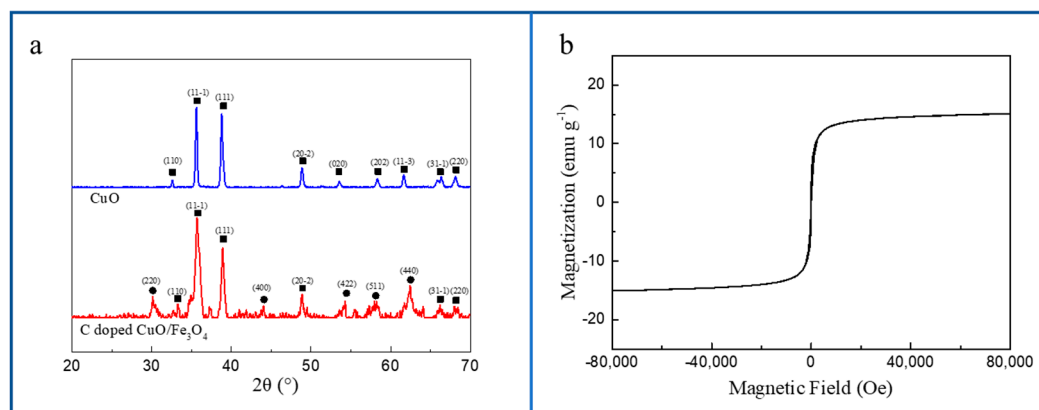

Figure 3. (**a**) Powder X-ray diffraction (PXRD) patterns of carbon-doped Fe_3O_4/CuO composite catalyst. (**b**) Magnetization curve at 300 K of carbon-doped Fe_3O_4/CuO composite catalyst.

The magnetic behavior of the carbon-doped Fe_3O_4/CuO composite catalyst sample was evaluated at 300 K. Its magnetization saturation value (Ms) was 15.1 emu·g^{-1}, suggesting a good magnetic property (Figure 3b). Thus, the magnetic carbon-doped Fe_3O_4/CuO composite catalyst could be readily separated from the reaction system using a magnet for the recycling process.

3.2. Catalytic Reduction

In this study, we investigated the application of carbon-doped CuO/Fe_3O_4 composite catalysts for the catalytic reduction of 4-nitrophenol. In Figure 4a, the results are shown for the catalytic reduction of 4-NP to 4-AP in the presence of $NaBH_4$ and carbon-doped CuO/Fe_3O_4 composite catalysts. The reduction process was followed based on the UV–Vis spectrophotometry. It shows that the absorbance at 400 nm (4-NP) decreased gradually as a function of time, while the absorbance at 290 nm (due to 4-AP) increased, confirming the catalytic reduction of 4-NP to 4-AP [44]. The catalytic reduction was almost complete within 10 min at room temperature, and the color of the solution changed from yellow to colorless. Similar results were also reported in the literature; Bordbar et al. [45] found that, using CuO/ZnO nanocomposites, catalytic reduction of 4-NP to 4-AP (using $NaBH_4$ as the reducing agent) was completed in several minutes.

The kinetics of calcined CMF, CuO, CuO/Fe_3O_4, and carbon-doped CuO/Fe_3O_4 composites are shown in Figure 4b. In the absence of catalyst, the reduction of 4-NP by $NaBH_4$ was negligible. In each case, the pseudo-first-order kinetic prevailed. The calcined CMF also had a negligible effect on the reduction of 4-NP. The rate constants (k) for CuO, CuO/Fe_3O_4, and carbon-doped CuO/Fe_3O_4 composite samples were 1.3×10^{-3} s^{-1}, 3.6×10^{-3} s^{-1} and 6.5×10^{-3} s^{-1}, respectively. In the case of CuO, the catalytic activity was the lowest due to the aggregation of CuO nanoparticles, while the catalytic efficiency of carbon-doped CuO/Fe_3O_4 composites was much better than that of CuO/Fe_3O_4, demonstrating that carbon doping is effective for enhancing the catalytic activity of the catalysts.

The catalytic reduction of 4-NP by $NaBH_4$ using metal-oxide nanoparticles (CuO) has two steps [46]: (1) borohydride ions are adsorbed onto the nanoparticle surface, forming active

surface-hydrogen, while 4-NP is also adsorbed onto the nanoparticle surface; (2) active hydrogen attacks the positively charged nitrogen in the nitro group of 4-NP, followed by the addition of two hydrogen atoms, producing 4-AP.
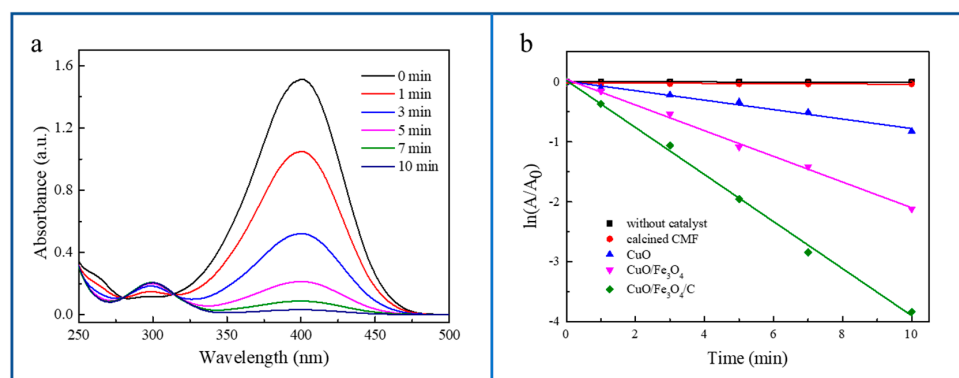

Figure 4. (**a**) Time-dependent ultraviolet–visible (UV–Vis) absorption spectra of 4-nitrophenol (4-NP) reduced by NaBH$_4$ in the presence of carbon-doped CuO/Fe$_3$O$_4$ composite catalysts; (**b**) the first-order kinetic plot (absorbance at 400 nm, ln(A$_t$/A$_0$)) versus reaction time for the reduction of 4-nitrophenol; A$_t$ and A$_0$ represent the absorbance values of 4-NP at 400 nm at designated time t and t = 0, respectively.

Cationic and anionic organic dyes were chosen to further investigate the catalytic properties of carbon-doped CuO/Fe$_3$O$_4$ composite catalyst. As shown in Figure 5a, for cationic dye (methylene blue), in the presence of NaBH$_4$ and carbon-doped CuO/Fe$_3$O$_4$ composite catalyst, the absorbance at 660 nm (MB) gradually decreased as a function of time; furthermore, the catalytic reduction was completed within 6 min at room temperature (the color of the solution was colorless).

The results from methyl orange (an anionic dye) are shown in Figure 5c. Under otherwise the same conditions, the color change (from orange to colorless) was slower than that for MB (Figure 5a, from blue to colorless). The pseudo-first-order rate law was also valid here (Figure 5d). For the carbon-doped CuO/Fe$_3$O$_4$ composite catalyst, the rate constant (k) was 2.4×10^{-3} s^{-1} for MO, while it was 12.9×10^{-3} s^{-1} for MB.

We compared the catalytic performance of the carbon-doped CuO/Fe$_3$O$_4$ composite catalyst for the reduction of 4-NP, MB, and MO, with other related ones from the literature (Table 1). As shown, the carbon-doped CuO/Fe$_3$O$_4$ composite catalyst showed much improved results, and the pseudo-first-order rate constant (k) for the nanocomposite catalyst from the present study was indeed consistently higher than that reported in the literature. The improved results may be attributed to the unique original morphologies associated with HKUST-1.

Table 1. Comparison of the catalytic performance for the reduction of 4-nitrophenol, methylene blue (MB), and methyl orange (MO) using the carbon-doped CuO/Fe$_3$O$_4$ composite catalyst and other reported catalysts in the literature. NP—nanoparticle.

| Pollutant	Samples	Concentration of Pollutant	Time (min)	k (s^{-1})	Reference
4-Nitrophenol	Agnp-PSAC	0.02 mM	25	3.9×10^{-3}	[47]
	CF-AuNPs	1 mM	11	0.17×10^{-3}	[48]
	CuO	0.1 mM	32	5.8×10^{-3}	[49]
	CuO/Fe$_3$O$_4$/C	1 mM	10	6.5×10^{-3}	This work
Methylene Blue	Au/Fe$_3$O$_4$@C	0.01 mM	10	5.5×10^{-3}	[50]
	AuNPs	1 mM	9	4.0×10^{-3}	[51]
	Fe$_3$O$_4$@polydopamine-Ag	0.1 mM	-	7.2×10^{-3}	[52]
	CuO/Fe$_3$O$_4$/C	0.03 mM	6	12.9×10^{-3}	This work
Methyl Orange	Ag–γ-Fe$_2$O$_3$	0.3 mM	30	1.53×10^{-3}	[53]
	Ag-CuO	0.006 mM	120	0.3×10^{-3}	[54]
	Ag@Fe	0.1 mM	14	1.6×10^{-3}	[55]
	CuO/Fe$_3$O$_4$/C	0.03 mM	25	2.4×10^{-3}	This work
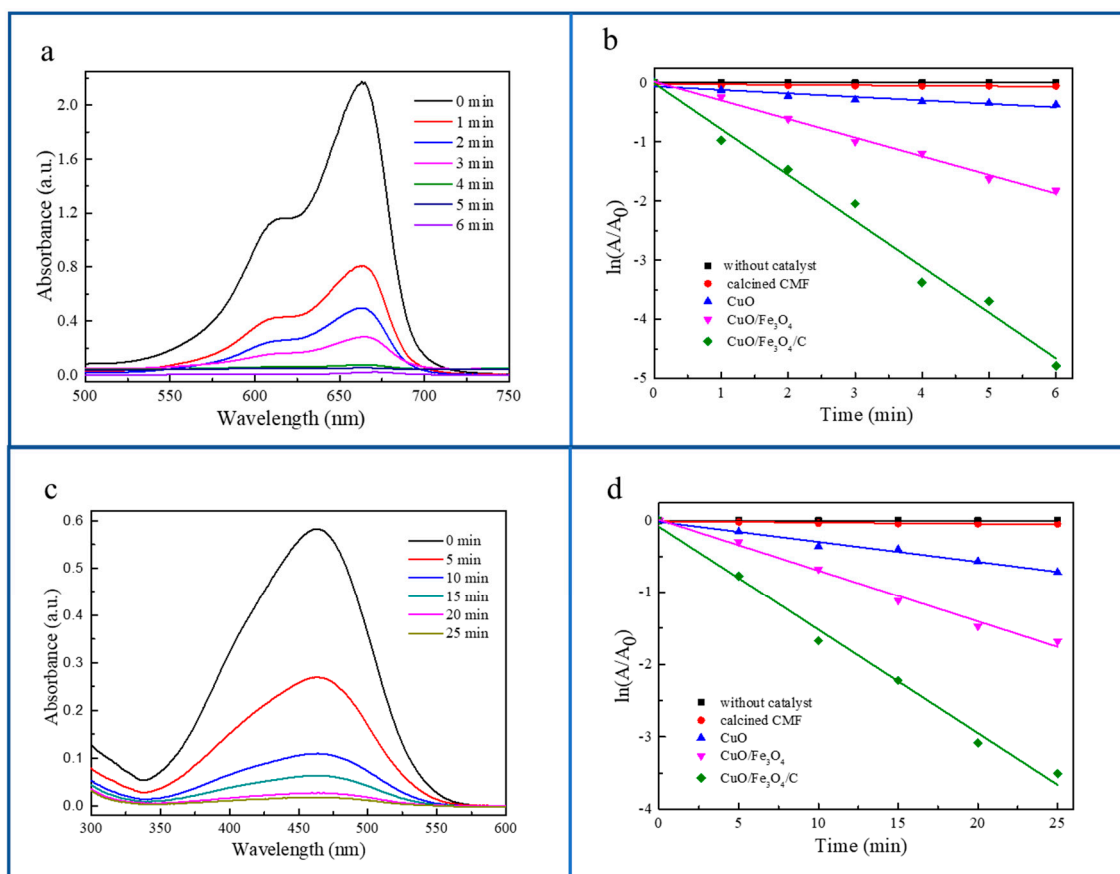
Figure 5. (**a**) Time-dependent UV–Vis absorption spectra of methylene blue (MB) with the carbon-doped CuO/Fe_3O_4 composite catalyst in the presence of $NaBH_4$; (**b**) the corresponding first-order kinetic plot (absorbance at 660 nm, $\ln(A_t/A_0)$) versus reaction time for the reduction of MB; A_t and A_0 represent the absorbance of MB (660 nm) at designated time t and t = 0, respectively; (**c**) time-dependent UV–Vis absorption spectra of methyl orange (MO) with the carbon-doped CuO/Fe_3O_4 composite catalyst in the presence of $NaBH_4$; (**d**) the corresponding first-order kinetic plot (absorbance at 460 nm, $\ln(A_t/A_0)$) versus reaction time for the reduction of MO; A_t and A_0 represent the absorbance of MO (460 nm) at designated time t and t = 0, respectively.

From the viewpoint of practical application, the recycling/reuse of the catalyst is of critical importance. In the present study, after the catalytic degradation experiments, the magnetic carbon-doped CuO/Fe_3O_4 composite catalyst was readily separated from the reaction system using an external magnet. The used catalysts were collected, and rinsed with distilled water several times. After a thorough washing process, the recovered magnetic catalyst was reused in the subsequent run of catalytic reduction of 4-NP under identical conditions, and the same process was repeated five times. The results are shown in Figure 6. The catalytic performance of the magnetic carbon-doped CuO/Fe_3O_4 composite catalyst decreased only slightly (the 4-NP reduction ratio decreased from 100% to 96%) after five cycles. Similar results were obtained in the reuse/recycling experiments of the as-prepared magnetic carbon-doped CuO/Fe_3O_4 composite catalyst during the catalytic reduction of MB and MO. Therefore, the as-prepared magnetic carbon-doped CuO/Fe_3O_4 composite catalyst is a promising system for practical applications.
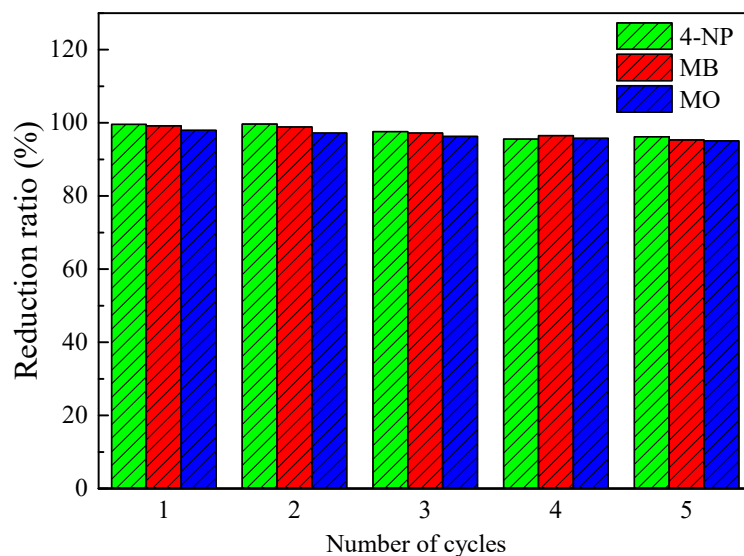
Figure 6. Reduction conversion ratio of 4-NP, MB, and MO after five successive cycles using the carbon-doped CuO/Fe$_3$O$_4$ catalyst.

4. Conclusions

In this study, a nano-cellulose/MOF-derived carbon-doped CuO/Fe$_3$O$_4$ composite catalyst was successfully fabricated through pyrolysis/thermolysis of the HKUST-1/Fe$_3$O$_4$/CMF composite. The resultant carbon-doped CuO/Fe$_3$O$_4$ composite catalyst took advantage of the original porous morphology of HKUST-1; consequently, the carbon-doped CuO/Fe$_3$O$_4$ composite catalyst exhibited high catalytic activity for the reduction of 4-NP and organic dyes (MB and MO). In addition, the carbon-doped CuO/Fe$_3$O$_4$ composite catalyst showed good reusability/recyclability after five cycles. Notably, this strategy can be extended to the preparation of other functional MOF-based derivatives.

Conflicts of Interest: The authors declare no conflicts of interest.

References

1. Almasi, H.; Jafarzadeh, P.; Mehryar, L. Fabrication of novel nanohybrids by impregnation of CuO nanoparticles into bacterial cellulose and chitosan nanofibers: Characterization, antimicrobial and release properties. *Carbohydr. Polym.* **2018**, *186*, 273–281. [CrossRef] [PubMed]

2. Palomo, J.M.; Filice, M. Biosynthesis of Metal Nanoparticles: Novel Efficient Heterogeneous Nanocatalysts. *Nanomaterials* **2016**, *6*, 84. [CrossRef] [PubMed]

3. Tran, C.D.; Makuvaza, J.; Munson, E.; Bennett, B. Biocompatible Copper Oxide Nanoparticle Composites from Cellulose and Chitosan: Facile Synthesis, Unique Structure, and Antimicrobial Activity. *ACS Appl. Mater. Interfaces* **2017**, *9*, 42503–42515. [CrossRef] [PubMed]

4. Müller, A.; Peglow, S.; Karnahl, M.; Kruth, A.; Junge, H.; Brüser, V.; Scheu, C. Morphology, optical properties and photocatalytic activity of photo-and plasma-deposited au and Au/Ag core/shell nanoparticles on titania layers. *Nanomaterials* **2018**, *8*, 502. [CrossRef] [PubMed]

5. Corma, A.; Garcia, H. Supported gold nanoparticles as catalysts for organic reactions. *Chem. Soc. Rev.* **2008**, *37*, 2096–2126. [CrossRef] [PubMed]

6. Gangula, A.; Podila, R.; Karanam, L.; Janardhana, C.; Rao, A.M. Catalytic Reduction of 4-Nitrophenol using Biogenic Gold and Silver Nanoparticles Derived from *Breynia rhamnoides*. *Langmuir* **2011**, *27*, 15268–15274. [CrossRef] [PubMed]

7. Huang, Z.; Cui, F.; Kang, H.; Chen, J.; Zhang, X.; Xia, C. Highly Dispersed Silica-Supported Copper Nanoparticles Prepared by Precipitation−Gel Method: A Simple but Efficient and Stable Catalyst for Glycerol Hydrogenolysis. *Chem. Mater.* **2008**, *20*, 5090–5099. [CrossRef]

8. Ma, J.; Sun, Z.; Wang, Z.; Zhou, X. Preparation of ZnO–cellulose nanocomposites by different cellulose solution systems with a colloid mill. *Cellulose* **2016**, *23*, 3703–3715. [CrossRef]

9. Aguirre, M.E.; Zhou, R.; Eugene, A.J.; Guzman, M.I.; Grela, M.A. Cu_2O/TiO_2 heterostructures for CO_2 reduction through a direct Z-scheme: Protecting Cu_2O from photocorrosion. *Appl. Catal. B Environ.* **2017**, *217*, 485–493. [CrossRef]

10. Zhou, R.; Guzman, M.I. Photocatalytic Reduction of Fumarate to Succinate on ZnS Mineral Surfaces. *J. Phys. Chem. C* **2016**, *120*, 7349–7357. [CrossRef]

11. Jiang, D.; Zhang, Y.; Li, X. Synergistic effects of CuO and Au nanodomains on Cu_2O cubes for improving photocatalytic activity and stability. *Chin. J. Catal.* **2019**, *40*, 105–113. [CrossRef]

12. Rodríguez, N.A.; Savateev, A.; Grela, M.A.; Dontsova, D. Facile Synthesis of Potassium Poly(heptazine imide) (PHIK)/Ti-Based Metal–Organic Framework (MIL-125-NH2) Composites for Photocatalytic Applications. *ACS Appl. Mater. Interfaces* **2017**, *9*, 22941–22949. [CrossRef] [PubMed]

13. Hu, J.; Chen, G.; Lo, I.M.C. Removal and recovery of Cr(VI) from wastewater by maghemite nanoparticles. *Water Res.* **2005**, *39*, 4528–4536. [CrossRef] [PubMed]

14. Simeonidis, K.; Mourdikoudis, S.; Kaprara, E.; Mitrakas, M.; Polavarapu, L. Inorganic engineered nanoparticles in drinking water treatment: A critical review. *Environ. Sci. Water Res. Technol.* **2016**, *2*, 43–70. [CrossRef]

15. Keller, A.A.; Wang, H.; Zhou, D.; Lenihan, H.S.; Cherr, G.; Cardinale, B.J.; Miller, R.; Ji, Z. Stability and Aggregation of Metal Oxide Nanoparticles in Natural Aqueous Matrices. *Environ. Sci. Technol.* **2010**, *44*, 1962–1967. [CrossRef] [PubMed]

16. Marambio-Jones, C.; Hoek, E.M.V. A review of the antibacterial effects of silver nanomaterials and potential implications for human health and the environment. *J. Nanopart. Res.* **2010**, *12*, 1531–1551. [CrossRef]

17. Su, X.; Kanjanawarut, R. Control of Metal Nanoparticles Aggregation and Dispersion by PNA and PNA−DNA Complexes, and Its Application for Colorimetric DNA Detection. *ACS Nano* **2009**, *3*, 2751–2759. [CrossRef]

18. Zhang, Q.; Lee, I.; Ge, J.; Zaera, F.; Yin, Y. Surface-Protected Etching of Mesoporous Oxide Shells for the Stabilization of Metal Nanocatalysts. *Adv. Funct. Mater.* **2010**, *20*, 2201–2214. [CrossRef]

19. Zhu, Q.-L.; Li, J.; Xu, Q. Immobilizing Metal Nanoparticles to Metal–Organic Frameworks with Size and Location Control for Optimizing Catalytic Performance. *J. Am. Chem. Soc.* **2013**, *135*, 10210–10213. [CrossRef]

20. Bak, W.; Soo Kim, H.; Chun, H.; Cheol Yoo, W. Facile synthesis of metal/metal oxide nanoparticles inside a nanoporous carbon matrix (M/MO@C) through the morphology-preserved transformation of metal–organic framework. *Chem. Commun.* **2015**, *51*, 7238–7241. [CrossRef]

21. Xia, W.; Zou, R.; An, L.; Xia, D.; Guo, S. A metal–organic framework route to in situ encapsulation of $Co@Co_3O_4@C$ core@bishell nanoparticles into a highly ordered porous carbon matrix for oxygen reduction. *Energy Environ. Sci.* **2015**, *8*, 568–576. [CrossRef]

22. Ennas, G.; Falqui, A.; Marras, S.; Sangregorio, C.; Marongiu, G. Influence of Metal Content on Size, Dispersion, and Magnetic Properties of Iron−Cobalt Alloy Nanoparticles Embedded in Silica Matrix. *Chem. Mater.* **2004**, *16*, 5659–5663. [CrossRef]

23. Obena, R.P.; Lin, P.C.; Lu, Y.W.; Li, I.C.; del Mundo, F.; Arco, S.D.; Nuesca, G.M.; Lin, C.-C.; Chen, Y.-J. Iron Oxide Nanomatrix Facilitating Metal Ionization in Matrix-Assisted Laser Desorption/Ionization Mass Spectrometry. *Anal. Chem.* **2011**, *83*, 9337–9343. [CrossRef] [PubMed]

24. Kaushik, M.; Moores, A. Review: Nanocelluloses as versatile supports for metal nanoparticles and their applications in catalysis. *Green Chem.* **2016**, *18*, 622–637. [CrossRef]

25. Budarin, V.L.; Clark, J.H.; Luque, R.; Macquarrie, D.J.; White, R.J. Palladium nanoparticles on polysaccharide-derived mesoporous materials and their catalytic performance in C–C coupling reactions. *Green Chem.* **2008**, *10*, 382–387. [CrossRef]

26. Zhang, Z.; Wang, Z. Diatomite-Supported Pd Nanoparticles: An Efficient Catalyst for Heck and Suzuki Reactions. *J. Org. Chem.* **2006**, *71*, 7485–7487. [CrossRef]

27. Niu, H.; Liu, S.; Cai, Y.; Wu, F.; Zhao, X. MOF derived porous carbon supported Cu/Cu_2O composite as high performance non-noble catalyst. *Microporous Mesoporous Mater.* **2016**, *219*, 48–53. [CrossRef]

28. Burtch, N.C.; Jasuja, H.; Walton, K.S. Water Stability and Adsorption in Metal–Organic Frameworks. *Chem. Rev.* **2014**, *114*, 10575–10612. [CrossRef]

29. Duan, C.; Meng, J.; Wang, X.; Meng, X.; Sun, X.; Xu, Y.; Zhao, W.; Ni, Y. Synthesis of novel cellulose-based antibacterial composites of Ag nanoparticles@ metal-organic frameworks@ carboxymethylated fibers. *Carbohydr. Polym.* **2018**, *193*, 82–88. [CrossRef]

30. Leo, P.; Orcajo, G.; Briones, D.; Calleja, G.; Sánchez-Sánchez, M.; Martínez, F. A recyclable Cu-MOF-74 catalyst for the ligand-free O-arylation reaction of 4-nitrobenzaldehyde and phenol. *Nanomaterials* **2017**, *7*, 149. [CrossRef]

31. Shen, K.; Chen, X.; Chen, J.; Li, Y. Development of MOF-Derived Carbon-Based Nanomaterials for Efficient Catalysis. *ACS Catal.* **2016**, *6*, 5887–5903. [CrossRef]

32. Li, H.; Ke, F.; Zhu, J. MOF-derived ultrathin cobalt phosphide nanosheets as efficient bifunctional hydrogen evolution reaction and oxygen evolution reaction electrocatalysts. *Nanomaterials* **2018**, *8*, 89. [CrossRef] [PubMed]

33. Ji, W.; Xu, Z.; Liu, P.; Zhang, S.; Zhou, W.; Li, H.; Zhang, T.; Li, L.; Lu, X.; Wu, J.; et al. Metal–Organic Framework Derivatives for Improving the Catalytic Activity of the CO Oxidation Reaction. *ACS Appl. Mater. Interfaces* **2017**, *9*, 15394–15398. [CrossRef] [PubMed]

34. Yang, S.J.; Im, J.H.; Kim, T.; Lee, K.; Park, C.R. MOF-derived ZnO and ZnO@C composites with high photocatalytic activity and adsorption capacity. *J. Hazard. Mater.* **2011**, *186*, 376–382. [CrossRef] [PubMed]

35. An, X.; Cheng, D.; Dai, L.; Wang, B.; Ocampo, H.J.; Nasrallah, J.; Jia, X.; Zou, J.; Long, Y.; Ni, Y. Synthesis of nano-fibrillated cellulose/magnetite/titanium dioxide ($NFC@Fe_3O_4@TNP$) nanocomposites and their application in the photocatalytic hydrogen generation. *Appl. Catal. B Environ.* **2017**, *206*, 53–64. [CrossRef]

36. Zhang, Y.-F.; Qiu, L.-G.; Yuan, Y.-P.; Zhu, Y.-J.; Jiang, X.; Xiao, J.-D. Magnetic $Fe_3O_4@C/Cu$ and $Fe_3O_4@CuO$ core–shell composites constructed from MOF-based materials and their photocatalytic properties under visible light. *Appl. Catal. B Environ.* **2014**, *144*, 863–869. [CrossRef]

37. An, X.; Long, Y.; Ni, Y. Cellulose nanocrystal/hexadecyltrimethylammonium bromide/silver nanoparticle composite as a catalyst for reduction of 4-nitrophenol. *Carbohydr. Polym.* **2017**, *156*, 253–258. [CrossRef] [PubMed]

38. Boruban, C.; Esenturk, E.N. Activated carbon-supported CuO nanoparticles: A hybrid material for carbon dioxide adsorption. *J. Nanopart. Res.* **2018**, *20*, 59. [CrossRef]

39. Gu, C.; Qi, R.; Wei, Y.; Zhang, X. Preparation and performances of nanorod-like inverse CeO_2–CuO catalysts derived from Ce-1,3,5-Benzene tricarboxylic acid for CO preferential oxidation. *React. Kinet. Mech. Catal.* **2018**, *124*, 651–667. [CrossRef]

40. Dong, X.-L.; Mou, X.-Y.; Ma, H.-C.; Zhang, X.-X.; Zhang, X.-F.; Sun, W.-J.; Ma, C.; Xue, M. Preparation of CdS–TiO_2/Fe_3O_4 photocatalyst and its photocatalytic properties. *J. Sol-Gel Sci. Technol.* **2013**, *66*, 231–237. [CrossRef]

41. Avgouropoulos, G.; Ioannides, T.; Matralis, H. Influence of the preparation method on the performance of CuO–CeO_2 catalysts for the selective oxidation of CO. *Appl. Catal. B Environ.* **2005**, *56*, 87–93. [CrossRef]

42. Kumar, R.V.; Diamant, Y.; Gedanken, A. Sonochemical Synthesis and Characterization of Nanometer-Size Transition Metal Oxides from Metal Acetates. *Chem. Mater.* **2000**, *12*, 2301–2305. [CrossRef]

43. Zhang, H.; Zheng, L.; Ouyang, X.; Ni, Y. Carbon doping of $Ti_{0.91}Co_{0.03}La_{0.06}O_2$ nanoparticles for enhancing room-temperature ferromagnetism using carboxymethyl cellulose as carbon source. *Ceram. Int.* **2018**, *44*, 15754–15763. [CrossRef]

44. Li, J.; Liu, C.; Liu, Y. Au/graphene hydrogel: Synthesis, characterization and its use for catalytic reduction of 4-nitrophenol. *J. Mater. Chem.* **2012**, *22*, 8426–8430. [CrossRef]

45. Bordbar, M.; Negahdar, N.; Nasrollahzadeh, M. Melissa Officinalis L. leaf extract assisted green synthesis of CuO/ZnO nanocomposite for the reduction of 4-nitrophenol and Rhodamine B. *Sep. Purif. Technol.* **2018**, *191*, 295–300. [CrossRef]

46. You, J.-G.; Shanmugam, C.; Liu, Y.-W.; Yu, C.-J.; Tseng, W.-L. Boosting catalytic activity of metal nanoparticles for 4-nitrophenol reduction: Modification of metal naoparticles with poly(diallyldimethylammonium chloride). *J. Hazard. Mater.* **2017**, *324*, 420–427. [CrossRef] [PubMed]

47. Nabil, B.; Ahmida, E.A.; Christine, C.; Julien, V.; Abdelkrim, A. Polyfunctional cotton fabrics with catalytic activity and antibacterial capacity. *Chem. Eng. J.* **2018**, *351*, 328–339. [CrossRef]

48. Bouazizi, N.; El achari, A.; Campagne, C.; Vieillard, J.; Azzouz, A. Copper oxide coated polyester fabrics with enhanced catalytic properties towards the reduction of 4-nitrophenol. *J. Mater. Sci. Mater. Electron.* **2018**, *29*, 10802–10813. [CrossRef]

49. Islam, M.T.; Dominguez, N.; Ahsan, M.A.; Dominguez-Cisneros, H.; Zuniga, P.; Alvarez, P.J.J.; Noveron, J.C. Sodium rhodizonate induced formation of gold nanoparticles supported on cellulose fibers for catalytic reduction of 4-nitrophenol and organic dyes. *J. Environ. Chem. Eng.* **2017**, *5*, 4185–4193. [CrossRef]

50. Gan, Z.; Zhao, A.; Zhang, M.; Tao, W.; Guo, H.; Gao, Q.; Mao, R.; Liu, E. Controlled synthesis of Au-loaded Fe$_3$O$_4$@C composite microspheres with superior SERS detection and catalytic degradation abilities for organic dyes. *Dalton Trans.* **2013**, *42*, 8597–8605. [CrossRef]

51. Afshar, S.; Samari Jahromi, H.; Jafari, N.; Ahmadi, Z.; Hakamizadeh, M. Degradation of malachite green oxalate by UV and visible lights irradiation using Pt/TiO$_2$/SiO$_2$ nanophotocatalyst. *Sci. Iran.* **2011**, *18*, 772–779. [CrossRef]

52. Ganapuram, B.R.; Alle, M.; Dadigala, R.; Dasari, A.; Maragoni, V.; Guttena, V. Catalytic reduction of methylene blue and Congo red dyes using green synthesized gold nanoparticles capped by salmalia malabarica gum. *Int. Nano Lett.* **2015**, *5*, 215–222. [CrossRef]

53. Sallam, S.A.; El-Subruiti, G.M.; Eltaweil, A.S. Facile Synthesis of Ag–γ-Fe$_2$O$_3$ Superior Nanocomposite for Catalytic Reduction of Nitroaromatic Compounds and Catalytic Degradation of Methyl Orange. *Catal. Lett.* **2018**, *148*, 3701–3714. [CrossRef]

54. Momeni, M.M.; Mirhosseini, M.; Mohammadi, N. Efficient photo catalytic degradation of methyl orange over Ag–CuO nanostructures grown on copper foil under visible light irradiation. *J. Mater. Sci. Mater. Electron.* **2016**, *27*, 6542–6551. [CrossRef]

55. Alzahrani, S.A.; Malik, M.A.; Al-Thabaiti, S.A.; Khan, Z. Seedless synthesis and efficient recyclable catalytic activity of Ag@Fe nanocomposites towards methyl orange. *Appl. Nanosci.* **2018**, *8*, 255–271. [CrossRef]